Asymmetry between Absorption and Photoluminescence Line Shapes of TPD: Spectroscopic Fingerprint of the Twisted Biphenyl Core

Reinhard Scholz,*,† Linus Gisslén,† Cameliu Himcinschi,‡,§ Igor Vragović,|| Eva M. Calzado,|| Enrique Louis,|| Emilio San Fabián Maroto,|| and María A. Díaz-García*,||

Walter Schottky Institut, Technische Universität München, D-85748 Garching, Germany, Max-Planck-Institut für Mikrostrukturphysik, D-06120 Halle, Germany, and Instituto Universitario de Materiales de Alicante and Unidad Asociada CSIC-UA, Universidad de Alicante, E-03080 Alicante, Spain

Received: August 4, 2008; Revised Manuscript Received: October 27, 2008

We analyze absorption, photoluminescence (PL), and resonant Raman spectra of *N*,*N*′-diphenyl-*N*,*N*′-bis(3-methylphenyl)-(1,1′-biphenyl)-4,4′-diamine (TPD), with the aim of providing a microscopic interpretation of a significant Stokes shift of about 0.5 eV that makes this material suitable for stimulated emission. The optical spectra were measured for TPD dissolved in toluene and chloroform, as well as for polystyrene films doped with varying amounts of TPD. In addition, we measured preresonant and resonant Raman spectra, giving direct access to the vibrational modes elongated in the relaxed excited geometry of the molecule. The experimental data are interpreted with calculations of the molecular geometry in the electronic ground state and the optically excited state using density functional theory. Several strongly elongated high-frequency modes within the carbon rings results in a vibronic progression with a calculated spacing of 158 meV, corroborated by the observation of vibrational sidebands in the PL spectra. The peculiarities of the potential energy surfaces related to a twisting around the central bond in the biphenyl core of TPD allow to quantify the asymmetry between the line shapes observed in absorption and emission.

1. Introduction

During the past decade, *N*,*N*′-diphenyl-*N*,*N*′-bis(3-methylphenyl)-(1,1′-biphenyl)-4,4′-diamine (TPD, see Figure 1) mainly attracted attention because of its transport properties, so that it became a prototypical hole-conducting compound used in multilayer light-emitting diodes.[1−3] Recent applications of TPD in UV detectors have revealed that the photoresponse is determined by the absorption coefficient of the material, even in blends with aluminum tris(8-hydroxyquinoline) (Alq_3).[4,5] Moreover, because of the very large Stokes shift of about 0.5 eV, TPD is transparent to its photoluminescence (PL), so that it has a promising potential for laser applications, showing stimulated emission even at high concentrations.[6−10] This finding is quite surprising, as most organic molecules with this property need to be diluted in a host matrix or in a solvent to show laser activity, given that, above a certain concentration, interactions between the molecules tend to quench PL and stimulated emission. Until now, only a few materials, such as thiophene-based oligomers[11−13] and several spiro-type materials,[14,15] have shown laser action in the form of neat films. Because, in all of those cases, the interchain interactions seem to play a major role in the luminescence and hence the laser properties of organic systems,[16] the study of the intermolecular interactions would be important to understanding their optical properties. For TPD, on the other hand, the intermolecular distances in the crystalline phase are rather large, without any evidence for stacking of the aromatic rings.[17] Therefore, it can be expected that, in the crystalline phase, intermolecular interactions play only a minor role for the photophysics.

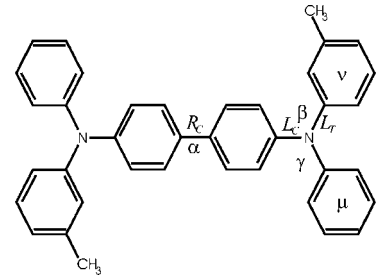

Figure 1. Trans isomer of *N*,*N*′-diphenyl-*N*,*N*′-bis(3-methylphenyl)-(1,1′-biphenyl)- 4,4′-diamine (TPD). The dihedral angles for the cis isomer are defined similarly.

Concerning the geometric structure and the frontier orbitals, some calculations have been performed using density functional theory (DFT), focusing on the hole-transport properties in the crystalline phase.[18−20] The objective of the present work was to analyze the optical properties of TPD with an ab initio interpretation of the experimentally observed Stokes shift, directly related to the possibility of observing stimulated emission even at high concentration. For that purpose, we extended our previous analysis of structural, energetic, and optical properties of TPD based on Hartree−Fock and related techniques such as configuration interaction of singles (CIS) to methods relying on DFT.[21,22]

In addition to performing a series of absorption and PL measurements at room temperature, we have used Raman spectroscopy to analyze the coupling between electronic excitations and internal vibrations. The high-frequency Raman-active modes contribute to the vibronic progression observed in PL, whereas the elongation of low-frequency modes results in a

* Corresponding authors. E-mail: reinhard.scholz@wsi.tum.de (R.S.), maria.diaz@ua.es (M.A.D.-G.).
† Technische Universität München.
‡ Present address: Institut für Physik, Technische Universität Chemnitz, D-09107 Chemnitz, Germany.
§ Max-Planck-Institut für Mikrostrukturphysik.
|| Universidad de Alicante.

10.1021/jp806939q CCC: $40.75
Published on Web 12/16/2008

substantial broadening of the vibronic subbands defined by the high-frequency modes. The experimental data were interpreted with the help of DFT calculations addressing the molecular geometry, the vertical excitation energies, the geometric rearrangement in the relaxed excited state, and the elongation of vibrational modes between the geometries in the relaxed excited state and the electronic ground state.

In section 2, we summarize the methods used in the present work before discussing the main results in section 3.

2. Computational Methods and Experimental Techniques

2.1. Geometry Optimization with Density Functional Theory. We carried out DFT calculations with the hybrid functional B3LYP[23,24] as implemented in the Turbomole 5.7 program package.[25] The molecular geometry was optimized at the B3LYP/DZ (double-ζ) level,[26] and the vertical excitation energy was obtained with time-dependent DFT (TD-DFT) in the adiabatic approximation, using the same functional and basis set.[27−31] The overall Stokes shift was obtained from a TD-DFT optimization of the geometry in the excited state,[32] and a projection of the deformation in the relaxed excited state onto the vibrational eigenvectors defined the Huang−Rhys factor S_k for each internal mode $\hbar\omega_k$.

2.2. Absorption and PL Spectra. We have measured linear absorption and PL at room temperature of TPD solutions in toluene and in chloroform in 1-cm-thick quartz cuvettes. Spectra of polystyrene (PS) films doped with varying amounts of TPD (between 5 and 100 wt % of the total mass) were also analyzed and compared. Films were deposited by spin-coating toluene solutions containing TPD and PS at a speed of 3000 rpm using an SMA-SPINNER 600Pro spinner. Absorption spectra were obtained with a Shimadzu spectrophotometer. PL was measured with a Jasco FP-6500/6600 fluorimeter, with the samples excited at 355 nm (3.49 eV), i.e., at the maximum of the lowest absorption band. PS and TPD (a mixture of cis and trans isomers) were purchased from Sigma-Aldrich and were used as received.

2.3. Raman Spectra. Preresonant Raman measurements were performed on a LabRam HR800 spectrometer (from Horiba Jobin Yvon) equipped with a liquid-nitrogen-cooled CCD detector (2048 × 512 pixels) and a 1800 groove/mm grating. The 514 nm (2.41 eV) emission line of an air-cooled Ar laser was used for excitation in a back-scattering geometry with both the incident and scattered beams passing the objective of the microscope. A 100× objective was used to focus the laser to a diameter of 1 μm on the sample surface, resulting in a power of 0.3 mW measured under the microscope objective. Each spectrum was obtained at room temperature by averaging 10 spectra recorded for 10 s each.

Resonant Raman measurements were performed in a back-scattering geometry with the same spectrometer, using a 2400 groove/mm grating and the 325 nm (3.81 eV) emission line of a He−Cd laser. As the resonant excitation tends to destroy the sample, the laser power had to be reduced to about 0.01 mW focused to a spot size of 1 μm on the sample surface. The larger noise resulting from the lower laser power was compensated by averaging 10 spectra recorded over a longer detection time of 120 s each.

2.4. Assignment of Raman Spectra. To assign the measured Raman-active modes to calculated internal vibrations, we determined their contributions to the reorganization energies. Based on eigenvectors of the internal vibrations and the equilibrium positions of all atoms j in the ground and excited states ($R_j^{(g)}$ and $R_j^{(e)}$) obtained with DFT and TD-DFT, we calculated the corresponding projections for each mode $\hbar\omega_k$.[33−35] This procedure defines the reorganization energy $\lambda_k^{(g)}$ on the potential energy surface (PES) of the electronic ground state, expressed in terms of the Huang−Rhys factor S_k of the mode

$$\lambda_k^{(g)} = S_k \hbar\omega_k \tag{1}$$

The values of the calculated frequencies were scaled down by a commonly used factor of 0.973 adequate for the B3LYP functional.[36] Keeping the reorganization energies fixed, the corresponding Huang−Rhys factors were thus multiplied by 1/0.973.

According to a derivation based on time correlators, the cross section for Stokes Raman scattering can be expressed as

$$\frac{d\sigma(\omega)}{d\Omega} \propto S_k[1 + n_{th}(\hbar\omega_k, k_B T)]|\Phi(\omega_L) - \Phi(\omega_s)|^2 \tag{2}$$

where Φ is the resonant part of the polarizability defined via a Kramers−Kronig transform of the absorption line shape; ω_L and ω_s are the frequencies of the laser light and the scattered radiation, respectively; and n_{th} is the thermal occupation of the vibrational mode with energy $\hbar\omega_k = \hbar\omega_L - \hbar\omega_s$.[37] This so-called transform theory of Raman cross sections has been applied successfully to cases with a rather structured absorption line shape, so that the difference between the polarizabilities at the laser frequency, ω_L, and at the frequency of the scattered light, ω_s, results in strongly modulated Raman excitation profiles.[38−41]

In the opposite limit of broad unmodulated absorption bands, it was demonstrated that transform theory according to eq 2 correctly predicts structureless Raman excitaton profiles resembling the absorption line shape.[42,43] In these cases, the difference between the polarizabilities in eq 2 can be replaced to leading order by the derivative at the midpoint between ω_L and ω_s

$$\Phi(\omega_L) - \Phi(\omega_s) \approx \omega_k \Phi'\left(\frac{\omega_L + \omega_s}{2}\right) \tag{3}$$

where the difference between incident and scattered frequencies has been expressed by the frequency of the excited vibration, $\omega_k = \omega_L - \omega_s$. Inserting this approximation into the Raman cross section, one finds

$$\frac{d\sigma(\omega)}{d\Omega} \propto S_k(\hbar\omega_k)^2[1 + n_{th}(\hbar\omega_k, k_B T)]|\Phi'\left(\omega_L - \frac{\omega_k}{2}\right)|^2 \tag{4}$$

In the preresonant case, the polarizability is dominated by the real part, with a functional form resembling a dispersive Lorentzian, so that the derivative Φ' depends on the detuning $\delta = \omega_{res} - (\omega_L - \omega_k/2)$ with respect to full resonance as

$$\Phi'\left(\omega_L - \frac{\omega_k}{2}\right) \propto \frac{1}{\delta^2} \tag{5}$$

Moreover, in cases with smooth structureless absorption bands with a width much larger than the frequency ω_k of the vibrational mode, even at resonance, the Raman cross section is essentially proportional to

$$\frac{d\sigma(\omega)}{d\Omega} \propto S_k(\hbar\omega_k)^2[1 + n_{th}(\hbar\omega_k, k_B T)] \tag{6}$$

with a further dependence on the mode k introduced only through the weakly frequency-dependent derivative of the polarizability in the form $|\Phi'(\omega_L - \omega_k/2)|^2$.

As discussed below, TPD has a broad absorption band composed of a strong transition between the highest occupied molecular oribital (HOMO) and lowest unoccupied molecular

oribital (LUMO) and weaker transitions about 0.5 eV higher in energy. Therefore, for the purposes of the present work, we consider the simple expression in eq 6 to be a valid approximation of the Raman cross sections, in both the preresonant and resonant cases.

In the relaxed excited geometry of TPD determined by TD-DFT, the dihedral angles are subject to large changes, especially for the twisting angle α within the biphenyl core. Therefore, in the excited geometry, the internal vibrations in the various rings take place in phenyl rings whose orientation no longer coincides with the electronic ground state, corresponding to a substantial Dushinsky rotation between the vibrational eigenvectors referring to the minima of the PES related to the ground and excited states. Because of these changes in the ring orientations, the projection of the deformation in the relaxed excited state onto the internal vibrations in the electronic ground state results in some nonorthogonality problems: The projection gives an undesired cross-talk between the relevant in-plane modes and C—H stretching modes, and similarly for torsional modes and low-frequency in-plane bending modes. As the Raman cross sections of high-frequency modes are determined on a very short time scale,[39] far below the time required for a substantial evolution of low-frequency torsional modes on the PES of the excited state, we defined an auxiliary excited geometry in which the dihedral angles are frozen according to the ground-state geometry but all bond lengths correspond to the relaxed excited geometry as determined by TD-DFT. As discussed below, this modified excited geometry gives Huang—Rhys factors of high-frequency in-plane modes in better agreement with the measured Raman spectra. We found this simple procedure based on frozen dihedral angles sufficient for the main purposes of the present investigation, avoiding a much more involved calculation accounting for the Dushinsky rotation.

2.5. Model Calculation of the Absorption and PL Line Shapes. Concerning the model calculation of the line shapes of absorption and PL, we have to distinguish between high-frequency internal modes arising from C—C stretching and C—H bending modes within the aromatic groups and low-frequency torsional modes, where the latter involve rigid rotations of the various phenyl groups against each other.

Along the elongation patterns of high-frequency modes, the contributions to $\lambda_k^{(g)}$ and $\lambda_k^{(e)}$ are similar, so that these modes can be treated with Franck—Condon and Huang—Rhys factors. As can be seen from the following sections, these modes occur in the range between 900 and 1610 cm^{-1}. We summarize them as an effective mode at 1278 cm^{-1} (158 meV) whose Huang—Rhys factor was obtained from a sum over the corresponding modes within the aforementioned frequency interval, $S_{eff} = \sum_k S_k$.

For low-frequency modes with $\hbar\omega_k \ll k_B T$, including especially those involving a twisting of the bond connecting the two rings of the central biphenyl group, we performed a detailed comparison of the elongation patterns and harmonic frequencies of the modes at the minimum of the PES of the excited state with the modes in the electronic ground state. For these modes, we found substantial differences, directly reflecting the dissimilar shapes of the two PESs along selected twisting angles, especially around the bond connecting the central biphenyl group. Therefore, instead of using the Huang—Rhys factors of these modes, we modeled the absorption and PL line shapes starting from a Boltzmann distribution over the twisting angle α around the central bond. The shape of the two PESs around this bond results directly in a large asymmetry between the density of states and broadenings involved in absorption and PL. This is also reflected in different contributions to the respective reorganization energies $\lambda^{(g)}$ and $\lambda^{(e)}$.

TABLE 1: Optimized Geometries of the Cis and Trans Isomers of TPD in Their Electronic Ground and Excited States Obtained at the B3LYP/DZ Level, Using DFT for the Electronic Ground State and TD-DFT for the Excited State[a]

isomer, state	R_c (Å)	α (deg)	β, γ (deg)	μ (deg)	ν (deg)
cis, ground	1.484	32.8	40.3	43.3	42.8
cis, excited	1.444	4.7	55.5	32.8	32.7
trans, ground	1.484	32.9	40.3	43.2	42.8
trans, excited	1.444	−3.5	53.6	33.3	33.3

[a] R_c, length of central bond; α, central dihedral angle; β and γ, dihedral angles of the terminal rings; ν and μ, torsion angles of the terminal rings. Compare Figure 1.

3. Results and Discussion

3.1. Optimized Geometries and Transition Energies. The notation for the dihedral angles in the molecular structure of TPD is displayed in Figure 1. TPD consists of a central biphenyl core and two twisted diphenylamine terminal wings. In the cis isomer, the methyl groups of the tolyl rings point into the same direction, whereas in the trans isomer, they are oriented along opposite directions.

The geometric parameters in the electronic ground state and in the lowest excited state of the cis and trans isomers are reported in Table 1. Among the various possible isomers, we chose the ones in which both angles β have the same sign, so that the point group of both the cis and the trans isomers is C_2. For other choices of the respective signs, this symmetry is reduced to C_1.

For both isomers, the twisting in the electronic ground state is quite pronounced, as shown by the large value of the central dihedral angle. The twisted geometry obtained with B3LYP/DZ is in a good agreement with the results of previous DFT calculations.[18,19,22] However, the calculated shape does not correspond precisely to the experimental structure in a crystalline environment, as obtained by X-ray diffraction measurements on single crystals.[17] In the crystalline phase, the peripheral wings adopt considerably different conformations, thus breaking the C_2 symmetry that the free molecule can realize. When excited, cis TPD becomes nearly planar, with the central angle reduced to 4.7° and with the central bond length significantly shortened (see Table 1). A similar tendency was observed already in our previous calculations based on Hartree—Fock, CIS and DFT[21,22] and in DFT calculations for the cationic molecule.[18] The change in the dihedral angle in the center of the molecule can be understood from the node patterns of the orbitals shown in Figures 2 and 3.

The HOMO has a node plane orthogonal to the central bond, so that a deviation from planarity reduces the energetic cost for this node. The LUMO, on the other hand, has a bonding lobe across the central bond, so that a coplanar arrangement of the biphenyl core is most favorable. When comparing the orbitals in the optimized geometries of the ground and excited states, one observes that, in the excited state, the LUMO spreads less over the peripheral phenyl groups because conjugation across the amine groups is reduced by the increase of the angles β and γ (compare Table 1). As both the HOMO and LUMO are mainly localized in the biphenyl core,[20,21,44,45] the geometric changes within this core have the dominant influence on the photophysics. Among the various dihedral angles, by far, the largest change in the excited state occurs for the twist angle α

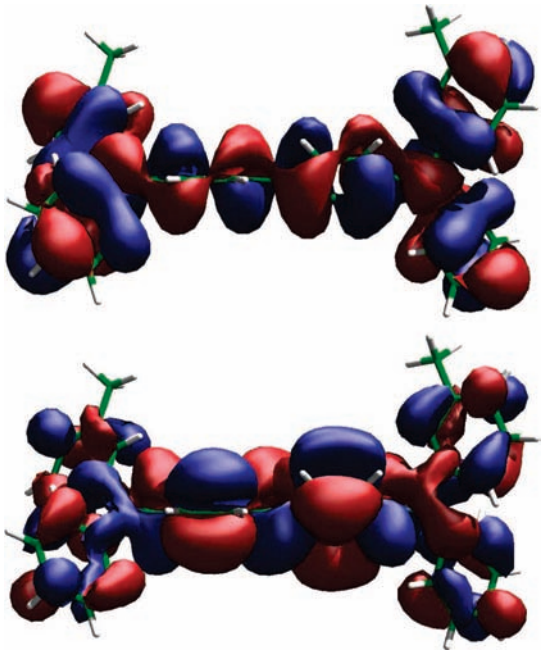

Figure 2. Frontier orbitals in the ground-state geometry of the cis isomer: (top) HOMO and (bottom) LUMO.

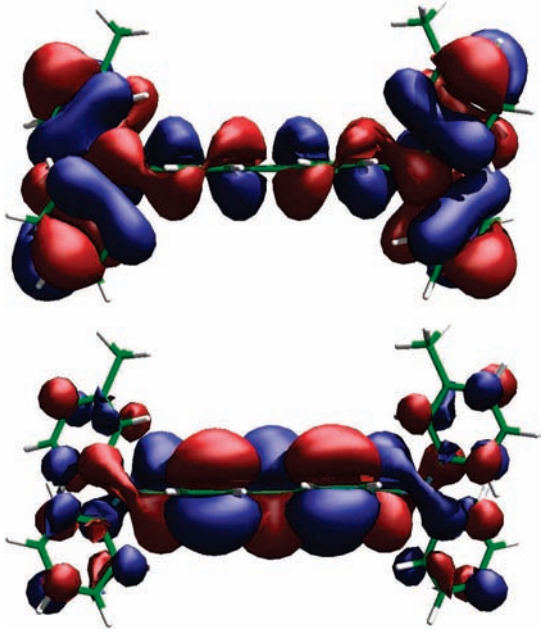

Figure 3. Frontier orbitals in the excited-state geometry of the cis isomer: (top) HOMO and (bottom) LUMO.

within the biphenyl group, so that this specific internal coordinate requires a rather detailed analysis.

In the electronic ground state, the dihedral angles of the trans isomer are very close to the respective angles of the cis isomer (compare Table 1). In the relaxed excited geometries of these isomers, both develop a nearly planar biphenyl core, but the peripheral groups are rotated farther from the orientiation of the central phenyl rings. As discussed below, the small differences between the geometric parameters of the two isomers do not induce major changes of the electronic transition energies.

3.2. Absorption and PL. The absorption spectra of TPD consist of two distinct peaks at 3.5 and 4 eV. The band at lower energy is always the dominant one, regardless of the type of solvent or substrate (see Figure 4). The PL is strongly red-

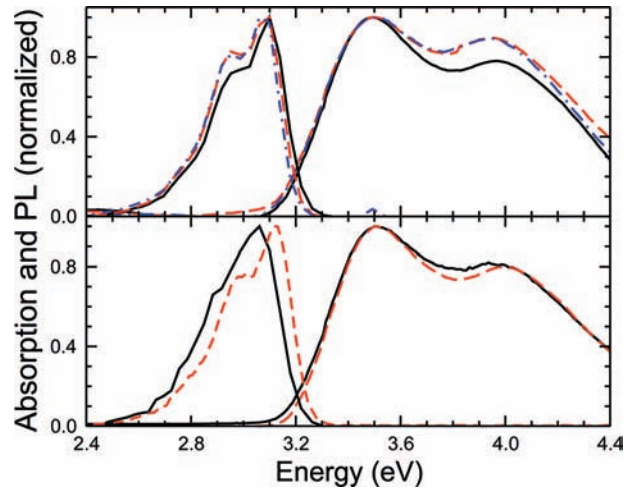

Figure 4. Measured linear absorption and PL of TPD at room temperature. (Top) PS films doped with varying amounts of TPD: 20%, solid black line; 50%, dashed red line; and 80%, dot-dashed blue line. (Bottom) TPD dissolved in chloroform (solid black line) and toluene (red dashed line) at a concentration of 5×10^{-5} mol/L in a 1-cm-thick quartz cuvette.

shifted, having a maximum around 3.1 eV followed by several shoulders at lower energy. As is shown below, these sidebands arise from a vibronic progression over an effective internal mode with $\hbar\omega_{\text{eff}} = 158$ meV (1278 cm^{-1}), calculated as an average over the most strongly elongated in-plane modes. In all solvents, the peaks of absorption and PL are clearly separated (see Figure 4). Taking the spectra for TPD dissolved in toluene as an example, the separation between the maxima of absorption and PL is about 0.38 eV, whereas the Stokes shift between the average over the first absorption peak and the center of mass of the PL band turns out to be about 0.57 eV, defined after eliminating the prefactors E in absorption and E^3 in PL, respectively.[46]

3.3. Transition Energies and Reorganization Processes. Contrary to our previous results obtained by HF methods that were dominated by the oscillator strength of the HOMO−LUMO transition,[21] the present TD-DFT analysis shows that additional transitions with significant coupling strengths occur below the measured ionization potential of 6.69 eV.[47] In the ground-state geometry, time-dependent DFT calculations at the B3LYP/DZ level find the lowest transition at 3.39 eV with an oscillator strength of $f_{\text{osc}} = 1.06$, as well as several transitions between 3.75 and 5 eV with a total oscillator strength of $f_{\text{osc}} = 0.65$ (compare Table 2). Although the sum of the strengths of the calculated transitions corresponds well to the intensity of the second band in absorption, the shape of this band cannot be reproduced, as these transitions are dispersed over a too large energetic region.

In previous Hartree−Fock-based calculations of the transition energies with configuration interaction of singles (CIS), the HOMO−LUMO transition was found at 5.61 eV, far above the observed value.[21] From TD-DFT calculations at the B3LYP/DZ level, one obtains the lowest transition energy in the ground-state geometry at 3.39 eV (compare Table 2), only about 0.1 eV below the maximum of the measured absorption. For de-excitation starting from the excited-state geometry, TD-DFT gives a vertical transition energy of 2.894 eV for the cis isomer and 2.910 eV for the trans isomer, about 0.2 eV below the maximum of the measured PL band (compare Table 3). The calculated Stokes shift of 0.496 eV for the cis isomer can be decomposed into a reorganization energy $\lambda^{(g)} = 0.224$ eV on

TABLE 2: Lowest Dipole-Active Transitions in the C_2-Symmetric Cis isomer of TPD, with Oscillator Strength $f_{osc} > 0.01$[a]

transition		energy (eV)	f_{osc} (1)
1*b*	(*y*)	3.39	1.059
1*a*	*z*	3.75	0.012
2*b*	(*x*)	3.83	0.014
3*b*	(*x*)	3.94	0.113
3*a*	*z*	3.94	0.231
4*a*	*z*	4.24	0.040
5*b*	(*y*)	4.35	0.014
6*b*	(*y*)	4.41	0.013
8*a*	*z*	4.46	0.086
7*b*	(*x*)	4.47	0.046
8*b*	(*y*)	4.79	0.052
10*b*	(*y*)	4.95	0.011

[a] For *a*-symmetric excitations, the transition dipole is oriented exactly along the $z(C_2)$ axis. For *b*-symmetric excitations, the orientation of the transition dipole is not defined by the C_2 point group. Therefore, the larger component of the transition dipole in the *xy* plane is given, where the *y* direction is oriented along the central bond of the biphenyl core.

TABLE 3: Energies (in eV) of the Potential Energy Surfaces in the Electronic Ground State and the Lowest Excited State, For the Relaxed Geometries of the Cis and Trans Isomers[a]

	geometry		
isomer, PES	ground	excited	reorganization energy
cis, ground	0.	0.224	0.224
cis, excited	3.390	3.118	0.272
cis, transition	3.390	2.894	0.496
trans, ground	0.	0.209	0.209
trans, excited	3.391	3.119	0.272
trans, transition	3.391	2.910	0.481

[a] Ground-state energies were obtained with DFT, and the excited-state energies were obtained with TD-DFT, both at the B3LYP/DZ level. For each isomer, the reference energy relates to the geometry in the electronic ground state. On an absolute scale, the ground-state energies of the two isomers differ by less than 1 meV.

the ground-state potential and $\lambda^{(e)} = 0.272$ eV on the excited-state potential. The large Stokes shift between the observed absorption and PL indicates that electronic and vibrational excitations in TPD are strongly coupled. This can be expected from the spatial distribution of HOMO and LUMO shown in Figures 2 and 3. They are delocalized mainly over the biphenyl core, which is strongly deformed in the relaxed excited geometry. The difference of 48 meV between the reorganization energies $\lambda^{(e)}$ and $\lambda^{(g)}$ is related to the different shapes of the PESs in the ground state and lowest excited state, involving especially the twisting around the central bond in the biphenyl core (compare sections 3.5 and 3.6).

The calculated reorganization energies of the trans isomer are very close to the respective values of the cis isomer (compare Table 3). With respect to the rather broad absorption and PL spectra in Figure 4, the differences between the calculated features of the two isomers are quite small, so that, in the remaining part of this work, we restrict our analysis to one specific isomer, choosing the cis form.

With respect to the observed Stokes shift of 0.57 eV for TPD in toluene, the value of 0.496 eV for the cis isomer resulting from TD-DFT shows a reasonable agreement. This is a substantial improvement over previous HF and CIS calculations, resulting in much larger values of $\lambda^{(g)} = 0.46$ eV, $\lambda^{(e)} = 0.62$ eV, and correspondingly a Stokes shift of 1.08 eV.[21]

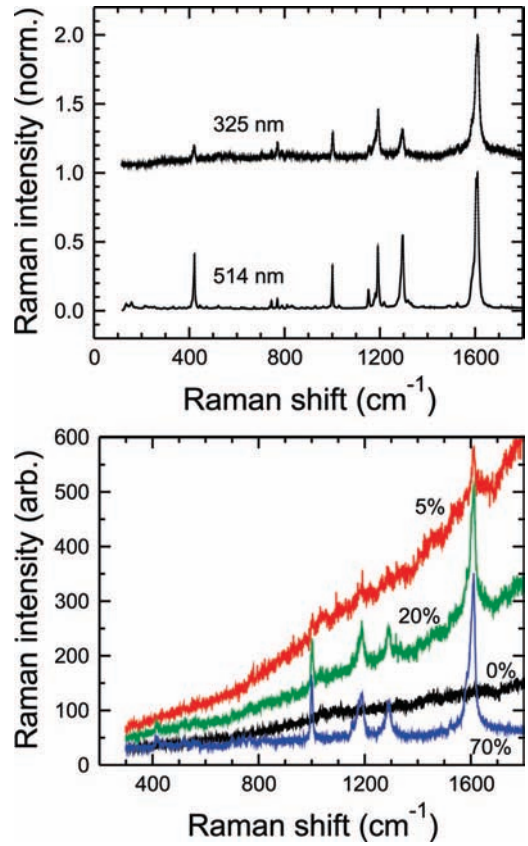

Figure 5. Raman spectra of pure TPD powder and of TPD-doped PS. (Top) Preresonant measurement of TPD powder using a laser line at 514 nm (2.41 eV) and resonant Raman spectra obtained with a laser line at 325 nm (3.81 eV). (Bottom) Resonant Raman spectra of TPD-doped PS films deposited on glass substrates, obtained with a laser line of 325 nm (3.81 eV). Black line, pure PS; red line, 5 wt % TPD; green line, 20 wt % TPD; and blue line, 70 wt % TPD.

In the following discussion, we do not attempt to reproduce quantitatively the second lower absorption feature at 4.0 eV. Instead, we demonstrate that the absorption band around 3.5 eV and the PL band can be obtained quantitatively from the following ingredients: a detailed analysis of the twisted biphenyl core, a Poisson progression over an effective mode at $\hbar\omega_{eff} = 158$ meV with $S_{eff} = 0.87$, a Gaussian broadening with fwhm $= 0.15$ eV, and a rigid red shift of the PL band arising from the elongation of low-frequency internal modes and reorganization processes within the solvation shell.

3.4. Preresonant and Resonant Raman Spectroscopy. We measured Raman spectra of both pure TPD powder and TPD embodied within PS films deposited on quartz and glass substrates (compare Figure 5). The spectra are dominated by several distinct peaks between about 1000 and 1600 cm^{-1}, with few features at frequencies below 500 cm^{-1} and a small contribution of high-frequency modes around 3000 cm^{-1} (not shown).

Comparing the Raman spectra for various concentrations of TPD in PS deposited on glass substrates (see Figure 5), we found that the dominant modes have practically the same frequencies and intensity patterns as for pure TPD. This indicates that, even at very high concentrations of TPD, the molecules interact only weakly, so that the photophysics of the internal vibrations are hardly modified. Similar spectra were also measured for TPD films deposited on quartz substrates.

The calculated resonant Raman spectra in Figure 6 are defined by eq 6 and visualized with a Lorentzian broadening of 10 cm^{-1}

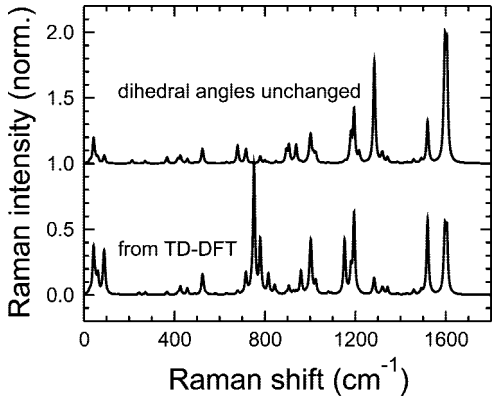

Figure 6. Resonant Raman spectra calculated according to eq 6, with B3LYP frequencies scaled down by a factor of 0.973. The computed spectra are visualized with Lorentzian line shapes with a fwhm of 10 cm^{-1}. (Bottom) As obtained from a projection of the TD-DFT deformation in the relaxed excited geometry onto the vibrational eigenvectors. (Top) From a modified excited geometry where changes of dihedral angles are eliminated. The curves are normalized to 1.

similar to the measured linewidths. The elongations of the internal modes in the relaxed excited geometry were obtained from two complementary projection schemes. First, the entire deformation in the relaxed excited geometry as obtained from the TD-DFT calculation was projected onto the vibrational eigenvectors, yielding the reorganization energies λ_k and the Huang−Rhys factors S_k reported in columns 2 and 3 of Table 4. However, from the very large changes of some dihedral angles in the excited geometry (compare Table 1), this projection scheme suffers from nonorthogonality problems related to the modified orientations of the various phenyl rings. The large change of the dihedral angle α produces a cross-talk between torsional modes, out-of-plane wagging modes, and low-frequency in-plane bending modes, resulting in rather large features in the range of 700−800 cm^{-1} where the experimental Raman spectra do not contain substantial cross sections.

To reduce artifacts of this type, we eliminated the changes of the dihedral angles from the excited geometry, so that all phenyl rings have essentially the same orientation as in the electronic ground state, but still with the internal deformations defined by the TD-DFT optimization of the relaxed excited geometry (compare the lower panel of Figure 7). The superimposed ground- and excited-state geometries reveal twisting elongations of C atoms on the central phenyl rings up to about 0.3 Å, as indicated in the upper panel of Figure 7. In section 3.6, we discuss why these elongations arising from a change of the dihedral angle α are highly relevant for the asymmetry between the line shapes of absorption and PL. Even though these elongations are very large, they remain far below the sum of the van der Waals radii of two atoms on neighboring molecules, so that we do not expect them to be influenced by intermolecular interactions. The elongations of the methyl groups attached to the peripheral rings are even larger, but because these groups have only a marginal influence on the spectroscopic properties, the possibility of an intermolecular steric hindrance inhibiting these elongations cannot result in a substantial influence on the photophysics.

The Raman cross sections of high-frequency modes are defined on a time scale faster than the twisting motion, so that they can be quantified from the modified excited geometry where the dihedral angles are frozen to their values in the electronic ground state. Columns 4 and 5 of Table 4 and Figure 6 demonstrate that this projection scheme improves the agreement with the measured Raman spectra in the range of 1002−1605 cm^{-1}, where the vibrations are dominated by elongation patterns in the plane of the various phenyl rings. The four strongest observed features at about 1600, 1296, 1186, and 1002 cm^{-1} are reproduced quantitatively, with a reasonable relative size of the respective cross sections.

A few modes receive cross sections that are much too large, including especially the vibration at 1524 cm^{-1} with an elongation pattern dominated by a stretching of the central bond in the biphenyl core. As this vibration is strongly coupled to changes of the dihedral angle α, its Raman cross section cannot be quantified with our projection schemes where dihedral angles and bond lengths are treated as orthogonal internal coordinates. In the region of the observed mode at 420 cm^{-1}, our calculations for the cis isomer do not result in substantial Raman cross sections. As six different isomers coincide in energy within 0.1

TABLE 4: Energies $\hbar\omega_k$, Reorganization Energies λ_k, and Huang−Rhys Factors of the Most Strongly Elongated Internal Modes[a]

B3LYP	TD-DFT		no twisting		experimental
$\hbar\omega_k$[b] (cm^{-1})	λ_k[b] (cm^{-1})	S_k[c] (1)	λ_k[c] (cm^{-1})	S_k (1)	$\hbar\omega_k$ (cm^{-1})
13	0.6	0.04	0.5	0.04	
26	29.7	1.13	27.5	1.05	
43	413.1	9.64	274.5	6.41	
52	85.1	1.64	40.7	0.78	
62	155.1	2.51	55.6	0.90	
88	156.9	1.79	15.7	0.18	
91	236.0	2.60	66.0	0.73	
214	0.4	0.00	24.8	0.12	
244	12.0	0.05	0.0	0.00	
272	15.0	0.06	17.7	0.07	
368	14.3	0.04	35.7	0.10	
416	7.8	0.02	23.1	0.06	
428	34.0	0.08	37.1	0.09	
459	24.8	0.05	21.9	0.05	
525	59.3	0.11	57.2	0.11	
529	23.5	0.04	14.4	0.03	
682	9.3	0.01	64.9	0.10	
719	52.1	0.07	47.9	0.07	
754	347.3	0.46	0.0	0.00	
782	138.0	0.18	22.1	0.03	785
818	49.1	0.06	2.9	0.00	
846	20.5	0.02	0.0	0.00	
898	4.0	0.00	34.5	0.04	
909	18.8	0.02	48.1	0.05	
941	5.3	0.01	48.9	0.05	
963	49.5	0.05	2.6	0.00	
1002	22.5	0.02	28.3	0.03	
1006	58.5	0.06	36.7	0.04	1002
1008	45.4	0.05	21.7	0.02	
1028	24.1	0.02	22.0	0.02	
1156	97.3	0.08	3.6	0.00	
1184	38.7	0.03	53.1	0.04	
1198	138.7	0.12	113.0	0.09	1186
1286	12.1	0.01	30.5	0.02	
1288	15.6	0.01	177.3	0.14	1296
1524	103.2	0.07	71.5	0.05	
1601	71.0	0.04	157.3	0.10	1596
1610	74.5	0.05	165.2	0.10	1606
2904	149.7	0.05	149.7	0.05	
3116	601.6	0.19	0.9	0.00	
3118	112.7	0.04	77.3	0.02	

[a] Data restricted to modes where the Huang-Rhys factor exceeds 0.02 in at least one of the projection schemes decribed in footnotes *b* and *c*. [b] Projection based on deformation in the relaxed excited geometry. [c] Projection based on a modified excited geometry where the changes of the dihedral angles with respect to the ground state geometry have been eliminated.

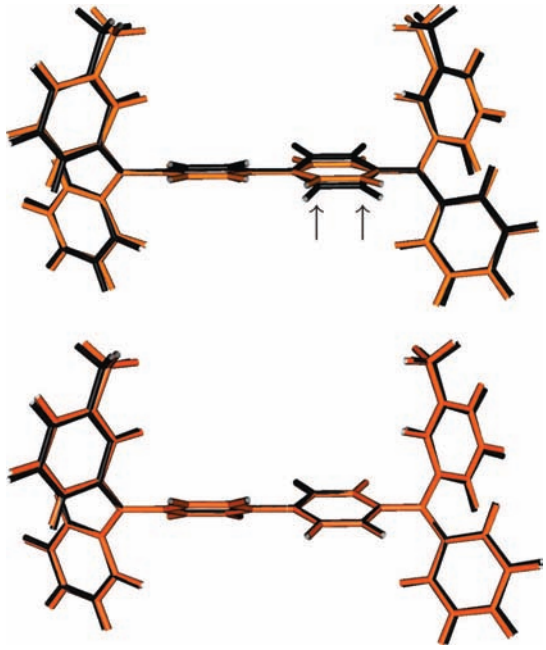

Figure 7. (Top) Excited-state geometry obtained from TD-DFT (orange) superimposed on the ground-state geometry (black), revealing large changes of the dihedral angles at the minimum of the excited PES and a corresponding out-of-plane elongation of carbon atoms in the central phenyl rings by about 0.3 Å (arrows). (Bottom) Modified excited-state geometry (orange) superimposed on the ground-state geometry, with internal deformations as obtained from the TD-DFT optimization of the excited-state geometry but dihedral angles fixed to their values in the electronic ground state. As all changes of bond lengths are below 3%, the visualization of the superimposed geometries can reveal changes only of dihedral angles and of the angles between the bonds surrounding the nitrogen atoms.

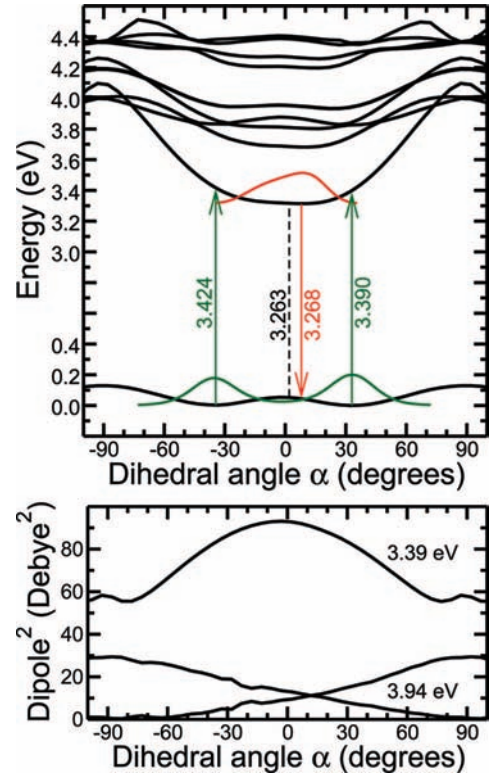

Figure 8. (Top) PES for rotation of the two halves of TPD around the dihedral angle α, for the electronic ground state and the lowest 10 excited states. The colored lines visualize Boltzmann distributions at $T = 300$ K around the minima of the lowest two PESs and the transition energies starting from the minima of the two PESs. The dashed vertical line indicates the lowest transition energy. (Bottom) Influence of the rotation around the central biphenyl bond on the square of the transition dipoles for the lowest three transitions with substantial coupling strength.

kcal mol^{-1} (4 meV),[19] we suppose that this feature arises from a different isomer.

Several modes at energies below 100 cm^{-1} acquire substantial reorganization energies. From a comparison of our two projection schemes and a visual inspection of the elongation patterns, we find that they are dominated by changes of the dihedral angles around the bonds connecting different phenyl rings, with torsional motion around the central bond playing the dominant role. For the calculated Raman cross sections of these torsional modes, it is essential to include the modified dihedral angles as obtained with TD-DFT. After eliminating the different orientations of the phenyl rings from the geometry of the relaxed excited state, the projection scheme yields strongly reduced Raman intensities of the low-frequency torsional modes.

3.5. Potential Energy Surfaces along Dihedral Angle α. In the electronic ground state, the PES for rotation of the two halves of the molecule against each other has two minima at $\alpha = 33°$ and $\alpha = -34°$ (compare Figure 8). The energies in the two minima are nearly degenerate, so that these geometries represent two of the various isomers of TPD. In the range $\alpha = 90-270°$ defining the trans isomer, the PESs look similar, so that we can restrict the following discussion to the range from $\alpha = -90°$ to $\alpha = 90°$ of the cis isomer displayed in Figure 8. The smallest excitation energy of 3.263 eV toward the lowest excited state occurs at $\alpha = 2°$, but the minimum of the lowest excited PES is placed at an angle of $\alpha = 8°$, with a slightly larger transition energy of 3.268 eV. This angle does not exactly coincide with the relaxed excited geometry reported in Table 1 because, in Figure 8, all other geometric parameters relate to the shape of the molecule in the electronic ground state. The small asymmetry of the PESs is also reflected in the Boltzmann distributions around their minima: The thermalized distribution in the electronic ground state has two maxima around $\alpha = 33°$ and $\alpha = -34°$, whereas in the lowest excited state, the thermalized distribution prior to radiative recombination looks like a skewed Gaussian with a maximum at $\alpha = 8°$.

The different curvatures of the two PESs result in a substantial difference between the reorganization energies along the dihedral angle α. The recombination from the minimum of the excited state gives a reorganization energy on the ground state PES of $\lambda^{(g)} = 46$ meV with respect to the absolute minimum at $\alpha = 33°$ and of $\lambda^{(g)} = 44$ meV with respect to the slightly shallower minimum at $\alpha = -34°$. Based on these values, the transition energies starting from the minima in the electronic ground state indicated in Figure 8a define reorganization energies of $\lambda^{(e)} = 76$ meV when starting at $\alpha = 33°$ and $\lambda^{(e)} = 112$ meV when starting at $\alpha = -34°$. Therefore, on average, the PES along the dihedral angle α gives a Stokes shift of $\lambda^{(e)} + \lambda^{(g)} = 139$ meV and an asymmetry between the reorganization energies of $\lambda^{(e)} - \lambda^{(g)} = 49$ meV, reproducing the difference between the total reorganization energies on the two PESs of 48 meV (compare the values for the cis isomer in Table 3). This excellent agreement indicates that the striking difference between the PESs depicted in Figure 8a is the key ingredient for quantifying the different line shapes of absorption and PL.

Figure 8b shows the dependence of the squared transition dipole moments on the dihedral angle α. For the lowest transition energy (3.39 eV in the ground-state geometry), the

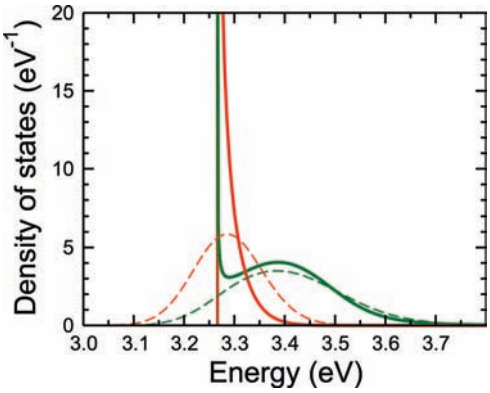

Figure 9. Density of states (DOS) for absorption (green) and emission (red), normalized to an area of 1. Each DOS is based on the Boltzmann distribution visualized in Figure 8a and the angular dependence of the squares of the transition dipoles in Figure 8b. The convolution of each DOS with a Gaussian of fwhm = 0.15 eV is shown as a dashed line.

square of the transition dipole varies by about one-quarter over the range of angles contributing to absorption and PL. Concerning the next-lowest transitions with a substantial coupling strength (3.94 eV in the ground-state geometry), two nearly degenerate transitions exchange coupling strength when the dihedral angle is varied, but the sum over the squared transition dipoles depends only weakly on this angle. These two transitions contribute about one-half to the observed strength of the second absorption band.

3.6. Model Calculation of Absorption and PL Spectra. The density of states (DOS) of the transition energies occurring at room temperature can be obtained from Boltzmann distributions over the dihedral angle α, as visualized in Figure 8a. These distributions have to be weighted by the inverse of the slope of the excitation energy, $(dE_{exc}/d\alpha)^{-1}$, and by the square of the transition dipole, resulting in the distribution over transition energies shown in Figure 9. At the lowest transition energy, E_{min}, occurring at α = 2°, the slope $dE_{exc}/d\alpha$ vanishes, producing a pole proportional to $1/(E - E_{min})^{1/2}$. For PL, this pole gives a substantial contribution to the entire area, and the integration over the thermal distribution increases the average PL energy by a value slightly below k_BT. The absorption line shape, on the other hand, is dominated by the dihedral angles where the thermalized distribution has its maxima, resulting in a broad absorption band around 3.41 eV. The singularity at the lowest transition energy cannot compensate for the lower part of the nearly Gaussian absorption band, which is cut off at the smallest transition energy, so that, for both absorption and PL, the DOS has a skewed shape with a flatter high-energy edge.

The DOS reported in Figure 9 is clearly much narrower than the observed spectra, raising the question of which broadening mechanisms have the largest influence. As demonstrated earlier for 3,4,9,10-perylene-tetracarboxylic-dianhydride (PTCDA), the large elongations of low-frequency internal vibrations and external phonons determine the line width of vibronic features related to high-frequency internal modes, where the latter are usually treated as the elongation of an effective mode.[48,49] In the case of TPD, several torsional modes below 100 cm^{-1} show extraordinarily large elongations. In the harmonic approximation, the contributions of their Poisson progressions to the first and second moments of the absorption line shape read

$$\langle E \rangle = \lambda^{(g)} = \sum_k S_k \hbar\omega_k \quad (7)$$

$$(\Delta E)^2 = \langle (E^2 - \langle E \rangle^2) \rangle = \sum_k S_k (\hbar\omega_k)^2 [1 + 2n(\hbar\omega_k, k_BT)] \quad (8)$$

Based on the projection scheme reported in columns 2 and 3 of Table 4, the modes below 100 cm^{-1} contribute $2\lambda^{(g)} = 267$ meV to the Stokes shift and a broadening of $\Delta E = [\langle (E^2 - \langle E \rangle^2) \rangle]^{1/2} = 83$ meV. Because of the very large Huang−Rhys factors involved, the shape of the Poisson progression of the most strongly elongated mode at 43 cm^{-1} resembles a Gaussian. Therefore, the simplest way to include a broadening in accordance with the above value for ΔE is to define a Gaussian with the same second moment. Parametrizing the latter as $\exp[-(E - \langle E \rangle)^2/2\sigma^2]$ so that it has $\Delta E = \sigma$, this gives a line width of fwhm = $2(2 \log 2\sigma)^{1/2} = 0.20$ eV, clearly much larger than the width of the DOS arising from the dihedral angle α alone.

To account for the residual part of the broadening not yet included in the previous analysis of the dihedral angle α, we convoluted the DOS in Figure 9 with a suitable Gaussian. The result of such a convolution using a Gaussian with fwhm = 0.15 eV is reported in Figure 9. In emission, the DOS arising from the twisting around the central bond remains so narrow that the convolution with the broader Gaussian essentially reproduces the shape of the latter, resulting in an emission band with a slightly increased broadening of fwhm = 0.16 eV. The DOS defining the absorption band already has a width of about fwhm = 0.22 eV, so that, after the convolution with the Gaussian, this value rises to fwhm = $[(0.22 \text{ eV})^2 + (0.15 \text{ eV})^2]^{1/2} = 0.27$ eV.

The above scheme conserves the asymmetry between the DOS responsible for absorption and PL in the form of a different line width. The average of the two values found, $\{[(0.27 \text{ eV})^2 + (0.16 \text{ eV})^2]/2\}^{1/2} = 0.22$ eV, turns out to be slightly larger than the line width of 0.20 eV expected from the lowest torsional modes only. This difference could easily be eliminated by convoluting with a somewhat narrower Gaussian, but as is shown below, the choice of a Gaussian with fwhm = 0.15 eV gives the best agreement with the observed PL data. The above reasoning demonstrates that about 90% of the line width obtained after the convolution arises in a natural way from the large elongations of the low-frequency torsional modes.

The third step of the model calculation is related to the high-frequency internal modes dominating the resonant Raman cross sections. Because the most strongly elongated modes occur between 1002 and 1605 cm^{-1}, we used their Huang−Rhys factors for the definition of an effective mode at $\hbar\omega_{eff} = \sum_k S_k \hbar\omega_k / \sum_k S_k = 1278$ cm^{-1} (158 meV) with $S_{eff} = \sum_k S_k = 0.87$, as obtained in the projection scheme after eliminating the changes of the dihedral angles from the excited-state geometry. The model curves in Figure 10 were obtained from a Poisson progression over this effective mode, where the shape of each vibronic subband was defined by the convolution of the respective DOS with a Gaussian of fwhm = 0.15 eV (compare Figure 9). Moreover, the resulting absorption and PL line shapes have been shifted rigidly by 175 meV against each other, essentially accounting for the part of the elongations of low-frequency torsional modes not included in the analysis of the PES along the dihedral angle. The calculated PL spectra have been multiplied by a factor of E^3 related to the density of photons.[46] As the above reasoning for the optical excitation defines the shape of the imaginary part of the dielectric function,

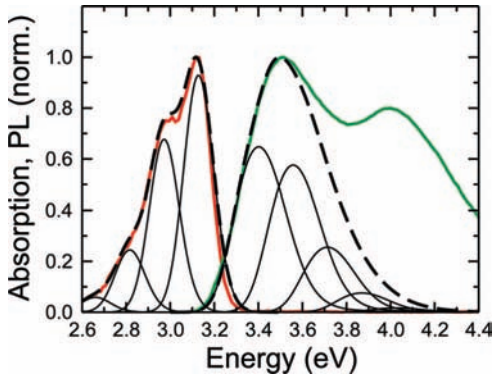

Figure 10. Comparison between the measured absorption and PL for TPD dissolved in toluene (green, absorption; red, PL) and the model calculation based on the dihedral angle α, a convolution with a Gaussian having a fwhm of 0.15 eV, a Poisson progression over an effective mode at 158 meV with a Huang−Rhys factor of 0.87, and a rigid shift of the absorption band by +13 meV and of the PL band by −162 meV (black, dashed line). In each case, the vibronic subbands resulting from a convolution of the DOS in Figure 9 with the Gaussian are shown separately (black thin lines). Altogether, the center of mass of the absorption band is shifted by +156 meV against the TD-DFT reference and the PL band by +81 meV.

$\mathcal{I}[\varepsilon(E)]$, the calculated absorption band reported in Figure 10 is proportional to $E.\mathcal{I}[\varepsilon(E)]$.

The detailed analysis of the potential landscape along the dihedral angle α including the averages over the thermal distributions gives a contribution of 121 meV to the total Stokes shift, and the effective mode contributes $2S_{\text{eff}}\hbar\omega_{\text{eff}} =$ 275 meV. As the TD-DFT calculation gives a total Stokes shift of 496 meV, all low-frequency modes included through neither the dihedral angle α nor the definition of the effective high-frequency mode should contribute 100 meV to the total Stokes shift. The difference between this value and the larger rigid shift of 175 meV applied in our model line shapes reflects the fact that the TD-DFT value of 496 meV for the Stokes shift is smaller than the observed value of about 0.57 eV. Deviations of TD-DFT reorganization energies in this range have to be expected, but a part of the observed Stokes shift might also be due to the solvation shell surrounding an excited TPD molecule in toluene: From Figure 4, it is clear that the Stokes shift varies with the surrounding solvent or matrix material.

In PL, the line shape used for each subband of the Poisson progression is so narrow that the vibronic progression remains visible, reproducing the observed weak modulation of the PL line shape at energies below its maximum (compare Figure 10). The DOS defining the absorption band already has a fwhm of about 0.22 eV (compare Figure 9). Therefore, after convoluting this curve with a Gaussian with fwhm = 0.15 eV, the resulting line shape has a fwhm as large as 0.27 eV for each vibronic subband, so that the expected vibronic peaks in absorption are totally washed out.

4. Concluding Remarks

In the present work, we have analyzed *N*,*N*′-diphenyl-*N*,*N*′-bis(3-methylphenyl)-(1,1′-biphenyl)-4,4′-diamine (TPD) with absorption, PL, and resonant Raman spectroscopy. The complementary information found with these methods was rationalized by a comprehensive analysis of the photophysics with time-dependent density functional calculations based on the B3LYP hybrid functional. It was found that the twisted shape of the central biphenyl group allows for an understanding of the different line widths observed in absorption and PL, together with the asymmetry between the reorganization energies on the two potential energy surfaces involved. The torsional modes at low frequencies contribute substantially to the broadening of absorption and PL. In fact, the vibronic subbands of a high-frequency effective mode defined as an average over the most strongly elongated high-frequency modes can be observed only in PL, but in absorption, the subbands are washed out by the larger broadening arising from the flat ground-state potential along the twisting around the central bond.

Our detailed model calculations have demonstrated that the photophysics of TPD can be understood from the properties of the molecule itself. The influence of intermolecular interactions is restricted to a small dependence of the Stokes shift on the solvent or matrix material, but the contribution of the surroundings to the broadening remains much smaller than the influence of the torsional modes of TPD at very low frequency.

Acknowledgment. We acknowledge support from the Spanish Ministry of Education, through Grant MAT2005-07369-C03-1 and the program "Juan de la Cierva", and from the University of Alicante. L.G. was supported by Project Scho 521/5 within the Scientific Priority Programme 1121 "Organic Field Effect Transistors: Structural and Dynamical Properties" funded by the Deutsche Forschungsgemeinschaft. The use of computational facilities at LRZ Garching and TU Chemnitz is gratefully acknowledged.

References and Notes

(1) Bulović, V.; Gu, G.; Burrows, P. E.; Forrest, S. R.; Thompson, M. E. *Nature* **1996**, *380*, 29.
(2) Borsenberger, P. M.; Weiss, D. S. *Organic Photoreceptors for Xerography*; Marcel Dekker: New York, 1998.
(3) Bellmann, E.; Shaheen, S. E.; Thayumanavan, S.; Barlow, S.; Grubbs, R. H.; Marder, S. R.; Kippelen, B; Peyghambarian, N. *Chem. Mater.* **1998**, *10*, 1668.
(4) Ray, D.; Patankar, M. P.; Döhler, G. H.; Narasimhan, K. L. *J. Appl. Phys.* **2006**, *100*, 113727.
(5) Ray, D.; Narasimhan, K. L. *Appl. Phys. Lett.* **2007**, *91*, 093516.
(6) Holzer, W.; Penzkofer, A.; Hörhold, H.-H. *Synth. Met.* **2000**, *113*, 281.
(7) Díaz-García, M. A.; de Ávila, S. F.; Kuzyk, M. *Appl. Phys. Lett.* **2002**, *80*, 4486.
(8) Díaz-García, M. A.; Calzado, E. M.; Villavilla, J. M.; Boj, P. G.; Quintana, J. A.; Kuzyk, M. *J. Nonlin. Opt. Phys. Mater.* **2004**, *13*, 621.
(9) Calzado, E. M.; Villavilla, J. M.; Boj, P. G.; Quintana, J. A.; Díaz-García, M. A. *J. Appl. Phys.* **2005**, *97*, 093103.
(10) Calzado, E. M.; Villavilla, J. M.; Boj, P. G.; Quintana, J. A.; Díaz-García, M. A. *Org. Electron.* **2006**, *7*, 319.
(11) Anni, M.; Gigli, G.; Cingolani, R.; Zavelani-Rossi, M.; Gadermaier, C.; Lanzani, G.; Barbarella, G.; Favaretto, L. *Appl. Phys. Lett.* **2001**, *78*, 2679.
(12) Zavelani-Rossi, M.; Lanzani, G.; De Silvestri, S.; Anni, M.; Gigli, G.; Cingolani, R.; Barbarella, G.; Favaretto, L. *Appl. Phys. Lett.* **2001**, *79*, 4082.
(13) Pisignano, D.; Anni, M.; Gigli, G.; Cingolani, R.; Zavelani-Rossi, M.; Lanzani, G.; Barbarella, G.; Favaretto, L. *Appl. Phys. Lett.* **2002**, *81*, 3543.
(14) Johansson, N.; Salbeck, J.; Bauer, J.; Weissörtel, F.; Bröms, P.; Andersson, A.; Salaneck, W. R. *Synth. Met.* **1999**, *101*, 405.
(15) Schneider, D.; Rabe, T.; Riedl, T.; Dobbertin, T.; Werner, O.; Kröger, M.; Becker, E.; Johannes, H.-H; Kowalsky, W.; Weimann, T.; Wang, J.; Hinze, P.; Gerhard, A.; Stössel, P.; Vestweber, H. *Appl. Phys. Lett.* **2004**, *84*, 4693.
(16) Cornil, J.; Beljonne, D.; Calbert, J. P.; Brédas, J. L. *Adv. Mater.* **2001**, *13*, 1053.
(17) Kennedy, A. R.; Smith, W. E.; Tackley, D. R.; David, W. I. F.; Shankland, K.; Brown, B.; Teat, S. J. *J. Mater. Chem.* **2002**, *12*, 168.
(18) Malagoli, M.; Brédas, J. L. *Chem. Phys. Lett.* **2000**, *327*, 13.
(19) Malagoli, M.; Manoharan, M.; Kippelen, B.; Brédas, J. L. *Chem. Phys. Lett.* **2002**, *354*, 283.

(20) Low, P. J.; Paterson, M. A. J.; Puschmann, H.; Goeta, A. E.; Howard, J. A. K.; Lambert, C.; Cherryman, J. C.; Tackley, D. R.; Leeming, S.; Brown, B. *Chem. Eur. J.* **2004**, *10*, 83.

(21) Vragović, I.; Calzado, E. M.; Díaz-García, M. A. *Chem. Phys.* **2007**, *332*, 48.

(22) Vragović, I.; Calzado, E. M.; Díaz-García, M. A.; Himcinschi, C.; Gisslen, L.; Scholz, R. *J. Lumin.* **2008**, *128*, 845.

(23) Becke, A. D. *Phys. Rev. A* **1988**, *38*, 3098.

(24) Lee, C.; Yang, W.; Parr, R. G. *Phys. Rev. B* **1988**, *37*, 785.

(25) Ahlrichs, R.; Bär, M.; Häser, M.; Horn, H.; Kölmel, C. *Chem. Phys. Lett.* **1989**, *162*, 165.

(26) Schäfer, A.; Horn, H.; Ahlrichs, R. *J. Chem. Phys.* **1992**, *97*, 2571.

(27) Runge, E.; Gross, E. K. U. *Phys. Rev. Lett.* **1984**, *52*, 997.

(28) Gross, E. K. U.; Kohn, W. *Adv. Quantum Chem.* **1990**, *21*, 255.

(29) *Density Functional Theory*; Gross, E. K. U., Driezler, R. M., Eds.; Plenum Press: New York, 1995; p 149.

(30) Casida, M. E. In *Recent Advances in Density Functional Methods*; Chong, D. P., Ed.; World Scientific: Singapore, 1995; Part I, p 115.

(31) (a) Furche, F.; Ahlrichs, A. *J. Chem. Phys.* **2002**, *117*, 7433. (b) , *J. Chem. Phys.* **2004**, *121*, 12772.

(32) Dierksen, M.; Grimme, S. *J. Phys. Chem. A* **2004**, *108*, 10225. *J. Chem. Phys.* **2004**, *120*, 3544.

(33) Brédas, J. L.; Beljonne, D.; Coropceanu, V.; Cornil, J. *Chem. Rev.* **2004**, *104*, 4971.

(34) Scholz, R.; Kobitski, A. Yu.; Kampen, T. U.; Schreiber, M.; Zahn, D. R. T. *Phys. Rev. B* **2000**, *61*, 13659.

(35) Marcus, R. A. *Rev. Mod. Phys.* **1993**, *65*, 599.

(36) Halls, M. D.; Velkovski, J.; Schlegel, H. B. *Theor. Chem. Acc.* **2001**, *105*, 413.

(37) Page, J. B.; Tonks, D. L. *J. Chem. Phys.* **1981**, *75*, 5694.

(38) Myers, A. B.; Mathies, R. A.; Tannot, D. J.; Heller, E. J. *J. Chem. Phys.* **1982**, *77*, 3857.

(39) Heller, E. J.; Sundberg, R. L.; Tannor, D. *J. Phys. Chem.* **1982**, *86*, 1822.

(40) (a) Brafman, O.; Chan, C. K.; Khodadoost, B.; Page, J. B.; Walker, C. T. *J. Chem. Phys.* **1984**, *80*, 5406. (b) Chan, C. K.; Page, J. B.; Tonks, D. L.; Brafman, O.; Khodadoost, B.; Walker, C. T. *J. Chem. Phys.* **1985**, *82*, 4813.

(41) Cable, J. R.; Albrecht, A. C. *J. Chem. Phys.* **1986**, *84*, 1969.

(42) Markel, F.; Ferris, N. S.; Gould, I. R.; Myers, A. B. *J. Am. Chem. Soc.* **1992**, *114*, 6208.

(43) Zhao, X.; Burt, J. A.; McHale, J. L. *J. Chem. Phys.* **2004**, *121*, 11195.

(44) Sugiyama, K.; Yoshimura, D.; Miyamae, T.; Miyazaki, T.; Ishii, H.; Ouchi, Y.; Seki, K. *J. Appl. Phys.* **1998**, *83*, 4928.

(45) Treuch, R.; Himpsel, F. J.; Kakar, S.; Terminello, L. J.; Heske, C.; van Buuren, T.; Dinh, V. V.; Lee, H. W.; Pakbaz, K.; Foz, G.; Jiménez, I. *J. Appl. Phys.* **1999**, *86*, 88.

(46) Loudon, R. *The Quantum Theory of Light*; Clarendon Press: Oxford, U.K., 1983; Chapter 4.10.

(47) Cornil, J.; Vanderdonckt, S.; Lazzaroni, R.; dos Santos, D. A.; Thys, G.; Geise, H. J.; Yu, L.-M.; Szablewski, M.; Bloor, D.; Lögdlund, M.; Salaneck, W. R.; Gruhn, N. E.; Lichtenberger, D. L.; Lee, P. A.; Armstrong, N. R.; Brédas, J. L. *Chem. Mater.* **1999**, *11*, 2436.

(48) Scholz, R.; Vragovic, I.; Kobitski, A. Yu.; Salvan, G.; Kampen, T. U.; Schreiber, M.; Zahn, D. R. T. In *Organic Nanostructures: Science and Applications*; Agranovich, V. M.; La Rocca, G. C., Eds.; IOS Press: Amsterdam, 2002; p 379.

(49) Scholz, R.; Schreiber, M. *Chem. Phys.* **2006**, *325*, 9.

JP806939Q